Boosting Anionic Redox Reactions of Li-Rich Cathodes through Lattice Oxygen and Li-Ion Kinetics Modulation in Working All-Solid-State Batteries

Shuo Sun, Chen-Zi Zhao, Gao-Yao Liu, Shu-Cheng Wang, Zhong-Heng Fu, Wei-Jin Kong, Jin-Liang Li, Xiang Chen, Xiangyu Zhao, and Qiang Zhang**

The use of lithium-rich manganese-based oxides (LRMOs) as the cathode in all-solid-state batteries (ASSBs) holds great potential for realizing high energy density over 600 Wh kg^{-1}. However, their implementation is significantly hindered by the sluggish kinetics and inferior reversibility of anionic redox reactions of oxygen in ASSBs. In this contribution, boron ions (B^{3+}) doping and 3D $Li_2B_4O_7$ (LBO) ionic networks construction are synchronously introduced into LRMO materials (LBO-LRMO) by mechanochemical and subsequent thermally driven diffusion method. Owing to the high binding energy of B—O and high-efficiency ionic networks of nanoscale LBO complex in cathode materials, the as-prepared LBO-LRMO displays highly reversible and activated anionic redox reactions in ASSBs. The designed LBO-LRMO interwoven structure enables robust phase and LBO-LRMO|solid electrolyte interface stability during cycling (over 80% capacity retention after 2000 cycles at 1.0 C with a voltage range of 2.2–4.7 V vs Li/Li$^+$). This contribution affords a fundamental understanding of the anionic redox reactions for LRMO in ASSBs and offers an effective strategy to realize highly activated and reversible oxygen redox reactions in LRMO-based ASSBs.

1. Introduction

With the broad applications of rechargeable batteries in our daily life, the research focus has shifted toward all-solid-state lithium batteries (ASSBs) that incorporate non-flammable solid electrolytes (SEs), offering enhanced safety and high energy density.[1–4] However, routine cathodes, exemplified by $LiCoO_2$ and $LiNi_{1-x-y}Mn_xCo_yO_2$ (NCM), exhibit limitations in energy density, failing to meet the escalating market demands for ASSBs. In comparison, lithium-rich manganese-based oxide (LRMO) cathode materials, have garnered extensive research attention due to their distinctive ability to utilize both anionic (oxygen) and cationic (transition metal, TM) redox reactions. This dual redox activity significantly amplifies their specific capacities, exceeding 250 mAh g^{-1}, effectively overcoming the limitations in capacity that are inherent to redox mechanisms reliant solely on TMs.[5–7] Furthermore, the tendency for TM ions to leach from the cathode into the liquid electrolytes (LEs)—a phenomenon detrimental to the capacity retention of LRMO cathodes—is significantly reduced in ASSBs. This mitigation enhances the viability of LRMO cathodes for ASSB development, as they offer the potential for high energy densities and improved cycling stability. Additionally, the use of LRMO is augmented by the environmental advantages and economic viability of manganese, which is not only abundant in the Earth's crust (≈950 ppm) but also non-toxic.[8–10] However, the practical application of LRMO cathodes in ASSBs faces significant challenges, including the difficulty in effectively activating anionic reactions and ensuring their irreversibility, which results in low specific capacity and poor cycling stability.[11–13]

In LRMO materials, the cationic and anionic redox reactions originate from the $LiTMO_2$ (TM = Ni, Co, Mn, etc.) and Li_2MnO_3 components, respectively. The distinctive anionic redox activity arises from the presence of residual lithium ions within TM layers, i.e., excess lithium content in a layered structure. This excess lithium facilitates the formation of new Li–O–Li and Li–O–□ (□; vacancy) local configurations, where oxygen electronic states, localized at elevated energy levels, are activated, thereby enabling lattice oxygen redox activity within the accessible

---

S. Sun, C.-Z. Zhao, W.-J. Kong, J.-L. Li, X. Chen, Q. Zhang
Tsinghua Center for Green Chemical Engineering Electrification
Beijing Key Laboratory of Green Chemical Reaction Engineering and Technology
Department of Chemical Engineering
Tsinghua University
Beijing 100084, China
E-mail: zcz@mail.tsinghua.edu.cn; zhang-qiang@mails.tsinghua.edu.cn

S. Sun, G.-Y. Liu, S.-C. Wang, X. Zhao
State Key Laboratory of Materials-Oriented Chemical Engineering
Jiangsu Collaborative Innovation Center for Advanced Inorganic Functional Composites
College of Materials Science and Engineering
Nanjing Tech University
Nanjing 211816, China

Z.-H. Fu
Beijing Advanced Innovation Center for Materials Genome Engineering
Institute for Advanced Materials and Technology
University of Science and Technology Beijing
Beijing 100083, China

Q. Zhang
Institute for Carbon Neutrality
Tsinghua University
Beijing 100084, China

The ORCID identification number(s) for the author(s) of this article can be found under https://doi.org/10.1002/adma.202414195

DOI: 10.1002/adma.202414195

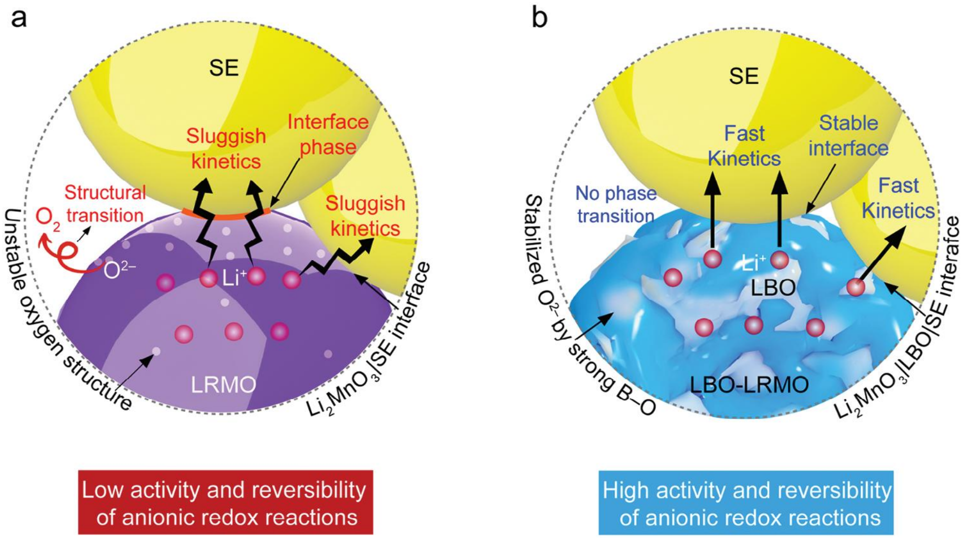

Figure 1. Schematic comparison of structures and anionic redox reactions of BM-LRMO and LBO-LRMO in ASSBs.

voltage range.[14] In liquid lithium batteries, LRMO is well infiltrated by the LEs, which enables the Li_2MnO_3|LE to have fast Li-ion transport kinetics. However, the poor contact between LRMO and SEs, combined with the low conductivity of the Li_2MnO_3, results in sluggish Li-ion transport kinetics at the Li_2MnO_3|SE interface (**Figure 1a**).[11,12,15,16] Additionally, the irreversibility of anionic redox reactions stems from the weak oxygen configuration, which facilitates O–O dimerization and the escape of oxygen during electrochemical processes.[17,18] Upon reacting with the SE, an irreversible interfacial phase forms, further increasing interfacial impedance and accelerating the degradation of the working batteries (Figure 1a). The lattice oxygen vacancies induced by the release of oxygen diffuse into the bulk, triggering an irreversible phase transition from layered phase to spinel phase. Such a process is also considered a major contributor to the degradation of ASSBs.[19–26] Therefore, simultaneous stabilization of the lattice oxygen structure and enhancement of Li-ion transport kinetics are essential for achieving high-efficiency anionic redox reactions, including highly reversible and active anionic redox.

Elemental doping is regarded to be an efficient approach to stabilize the anionic redox reactions.[27] Among various elements, the boron stands out for its high binding energy with oxygen. The strong B–O bonds effectively stabilize the oxygen ions, preventing excessive oxidation at high voltages. For instance, B-doping in O3-$NaLi_{1/9}Ni_{2/9}Fe_{2/9}Mn_{4/9}O_2$ was found to form the covalent B–O bonds and enhance the negative charges of the oxygen, thereby reinforcing the ligand framework and effectively inhibiting irreversible oxygen release.[28] Incorporating boron into the Li-rich cathode forms B–O bonds that are significantly stronger than the lattice Mn–O bonds, reducing the energy of the O 2p states and improving the reversibility of lattice oxygen redox reactions.[29] However, simple B-ion doping in LRMO materials is insufficient to improve the interfacial Li-ion transport kinetics within the cathode composites, resulting in low anionic redox activity in working ASSBs. Consequently, it is imperative to seek an effective strategy to simultaneously activate and stabilize anionic redox reactions.

In this contribution, we present a one-step strategy for incorporating B^{3+} into the lattice structures, coupled with the integration of 3D Li-ion networks from amorphous $Li_2B_4O_7$ (LBO) among the LRMO (LBO-LRMO) cathode materials. This process is achieved through solid-state mechanochemistry followed by a subsequent annealing treatment. Within the LBO-LRMO intertwined structure, LRMO domains seamlessly integrate with the soft, amorphous LBO domains throughout the entire framework, where strong B–O bonds are generated in the LRMO domains (Figure 1b). The simultaneous enhancement in Li-ion transport kinetics and thermodynamics stability of the oxygen structure leads to a multi-effect improvement in anionic redox activity and reversibility. A comprehensive analysis combining density functional theory (DFT) calculations, in situ galvanostatic electrochemical impedance spectra (GEIS), the distribution of relaxation time (DRT) technique, and time-of-flight secondary ion mass spectrometry (TOF-SIMS) demonstrates that anionic redox activity is significantly enhanced, while irreversible oxygen release from the lattice during deep delithiation is effectively suppressed. Benefiting from the improved structure of LRMO and LRMO|SE interface stability, the LBO-LRMO based ASSBs exhibit excellent long-cycling stability with ≈80.6% capacity retention after 2000 cycles at 1.0 C.

2. Results and Discussion

2.1. Theoretical Calculation of the Boron-Doped Oxide Compounds

The effect of B doping on the stability of the anionic redox process was revealed by theoretical calculations. Bond length and Bader charge analyses were employed to elucidate the impact of ion doping on the oxygen configuration of Li_2MnO_3 (**Figure 2a**). Notably, the average length of the B–O bond in B-doped Li_2MnO_3 is 1.28 Å, which is much smaller than those of Mn–O bond (1.90 Å), P–O bond (1.56 Å), S–O bond (1.50 Å), Si–O bond (1.75 Å), and Al–O bond (1.90 Å). This indicates that the incorporation

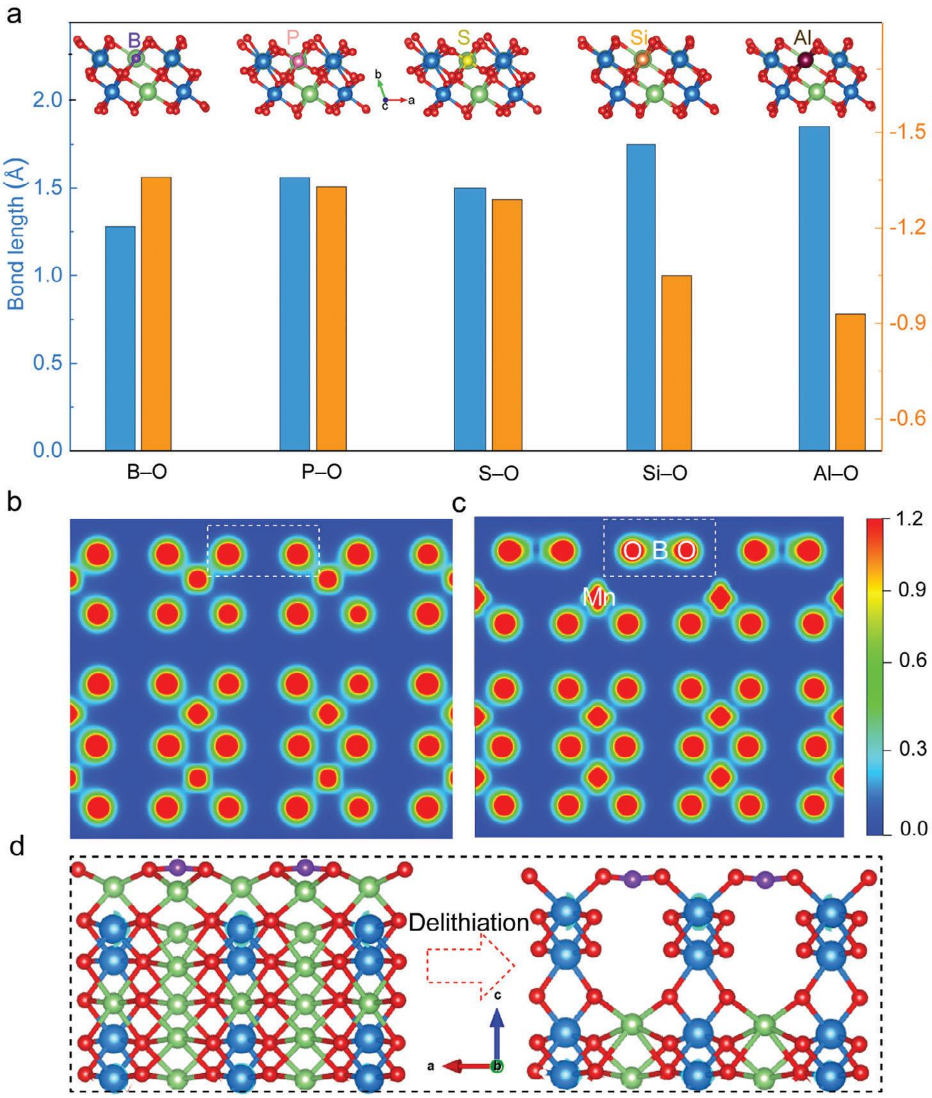

Figure 2. DFT calculation analysis. a) The average bond length and Bader charge of the B–O, P–O, S–O, Si–O, and Al–O in Li_2MnO_3. The shortest bond length of B–O and the most negative charge around the O for the B^{3+} prove that the incorporation of B^{3+} is optimal for stabilizing the oxygen ligand framework. Contour maps of charge density in (b) Li_2MnO_3 and c) B-doped Li_2MnO_3. d) The atomic structure of the (010) surface with the stabilized oxygen by formed strong B–O bonds during the delithiation. The blue, green, red, and purple spheres represent Mn, Li, O, and B atoms, respectively.

of B^{3+} into the Li_2MnO_3 can significantly reinforce the O ligand framework, which is further substantiated by the most negative charge around the O atoms in B-doped Li_2MnO_3. This robust framework can resist excessive oxidation of O^{2-} during high-voltage charging.[28,30] Charge density analysis further reveals that B-doped Li_2MnO_3 exhibits a stronger B–O covalent bond, with additional electrons being transferred to the oxygen atom (Figure 2b,c; Figure S1, Supporting Information), which is consistent with the bond length calculations. To simulate the delithiation state, several layers of Li ions at the surface of Li_2MnO_3 were removed. The O configuration changes significantly and spontaneously, forming the new O–O dimers structure during the delithiation process (Figure S2, Supporting Information). However, upon introducing the B–O bond, the formation process of O–O dimers during delithiation was not observed (Figure 2d), demonstrating that B-doping effectively reinforces the O ligand framework, which prevents over-oxidation of oxygen and therefore enhances structural stability.[8,14]

2.2. The Structure Characterization of LBO-LRMO Cathodes

The process of fabricating LBO-LRMO by using high-energy ball milling and subsequent thermally driven diffusion is schematically illustrated in Figure S3 (Supporting Information). During the ball-milling process, the LRMO secondary particles are dissociated into nanoparticles. As shown in Figures S4 and S5 (Supporting Information), morphologies of polycrystalline LRMO, BM-LRMO, and LBO-LRMO samples were observed by field emission scanning electron microscopy (SEM). Obviously, the precursor LRMO secondary particles are dissociated into nanoparticles by mechanical force. Meanwhile, the high-energy

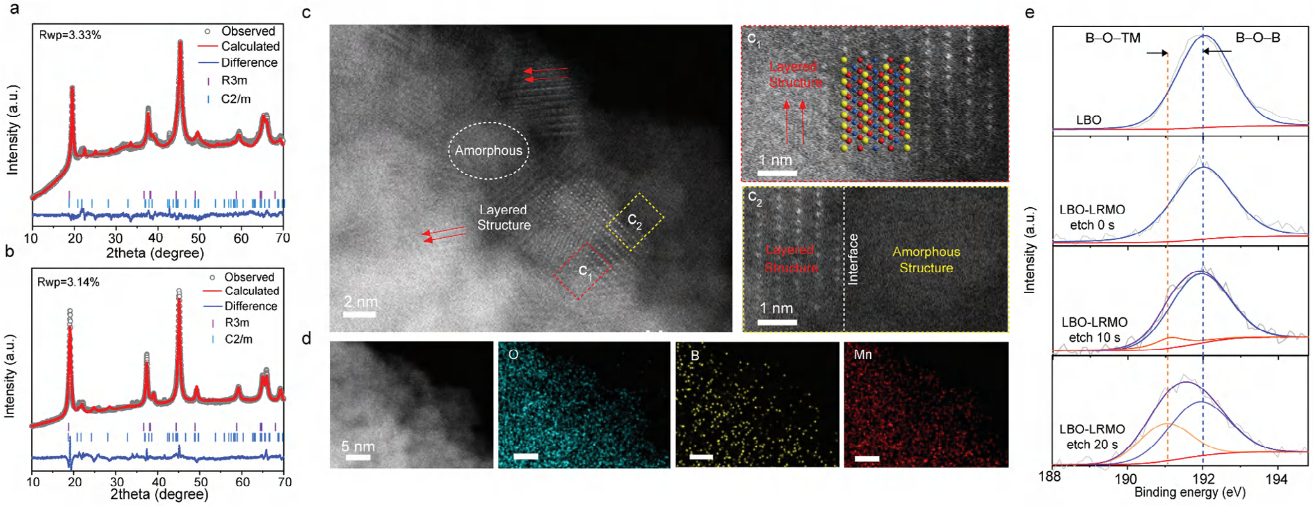

Figure 3. The structure analysis of the active cathode materials. a,b) Rietveld-refined XRD patterns of the BM-LBO and LBO-LRMO materials. c) HAADF-STEM image for intertwined LBO-LRMO. d) Energy-dispersive spectroscopy (EDS) mappings of O, B, and Mn of LBO-LRMO. e) B1s XPS spectra for LBO-LRMO materials after different etch time.

ball milling embeds nanoscale LBO into the interior of the LRMO nanoparticles, forming an interwoven LRMO and LBO structure and a large number of nanoscale interfaces. In addition, both mechanical forces and thermal diffusion drive solid-state reactions between LBO and LRMO, resulting in the gradient doping of B in the LRMO.[31] Amorphous LBO, being a soft oxide[31,32] and Li$^+$-conductor,[33,34] facilitates the formation of well-connected LRMO|LRMO and LRMO|SE interfaces and therefore benefits the Li-ion transport at the working interfaces. Therefore, the unique structure incorporates strongly covalent B–O bonds and amorphous LBO frameworks, leading to a stable oxygen configuration and enhanced anionic redox kinetics of LRMO.

X-ray diffraction (XRD) analysis along with Rietveld refinement was conducted to characterize the crystal structure of the BM-LRMO and LBO-LRMO. The XRD patterns for both LRMO and LBO-LRMO are indexed to the layered α-NaFeO$_2$ structure, which belongs to the $R\bar{3}m$ space group.[35] Weak superlattice reflection peaks corresponding to the Li$_2$MnO$_3$ phase in the C2/m space group are observed ranging from 20° to 25° (Figure S6, Supporting Information). These indicate the LRMO phases are well-preserved after treatment, while the LBO phase remains amorphous.[31] **Figure** 3a,b displays the Rietveld refinement of the XRD patterns of the BM-LRMO and LBO-LRMO materials. The calculated XRD patterns agree well with the experimental data with reliability indexes (R_{wp}) of 3.33% and 3.14% for the BM-LRMO and LBO-LRMO, respectively. Low deviation again confirms the distribution of LBO in the form of amorphous after ball-milling and annealing treatment. The refined cell parameters and atomic positions based on XRD are present in Tables S1 and S2 (Supporting Information). As shown in Table S2 (Supporting Information), the atomic percentage of B^{3+} in the Li and TM layers for the LiTMO$_2$ phase was determined to be 5.4% and 0%, respectively. For the Li$_2$MnO$_3$ phase, the atomic percentage of B^{3+} in the Li and TM layers was found to be 7.5% and 0%, respectively. Therefore, it can be confirmed that the doping site of B^{3+} in LBO-LRMO is in the Li layers. More atomic-level structural details and chemical features are analyzed by using high-angle annular dark-field scanning TEM (HAADF-STEM) techniques.

Magnified HAADF-STEM images in Figure 3c display an intertwined atomic structure (layered and amorphous domains), suggesting the nanoscale LRMO domains are surrounded by the amorphous LBO domains. The lattice fringe corresponds to the (003) planes of the layered structure, around which amorphous LRMO and LBO are interspersed. To directly check the existence of LBO, a high-resolution energy-dispersive spectroscopy (EDS) mapping was utilized. As depicted in Figure 3d and Figures S7 and S8 (Supporting Information), the EDS mappings demonstrate a homogeneous distribution of Mn, Co, Ni, O, and B within the LBO-LRMO. In addition, the core-level XPS spectra were conducted to accurately track the changes in their chemical environment. Through XPS depth analysis, the chemical environment of the LBO and LRMO was examined, with Ar ion etching applied to LBO-LRMO particles. As depicted in Figure 3e, the B–O–B signal located at 192.0 eV is observed in pure LBO and on the LBO-LRMO surface, suggesting the presence of LBO at the surface of LBO-LRMO particles. With etching from 0 to 20 s, a new TM–O–B peak emerges at ≈191.1 eV, growing continuously from the surface to the bulk, which demonstrates the B doping in LRMO.[36,37] When the etching duration reaches 50 s, the TM–O–B peak ratio remains similar to that observed at 20 s, signifying a uniform doping distribution in the bulk lattice of nanoscale LRMO (Figure S9, Supporting Information). After doping, as shown in Figure S10 (Supporting Information), the valence of the Mn ions is reduced from the surface to the bulk, while no valence change in Co and Ni is detected. The TOF-SIMS data show a precise overlap between the BO$^-$ and MnO$^-$ signals, providing strong evidence for the uniform distribution of B^{3+} within the LRMO bulk and the formation of B–O bonds (Figure S11a,b, Supporting Information). The BO$^-$ signal, observed in close proximity to the MnO$^-$ fragment, further indicates an interwoven structure between the LBO and LRMO materials. High-resolution 3D depth profiling (Figure S11c, Supporting Information) reveals a consistent

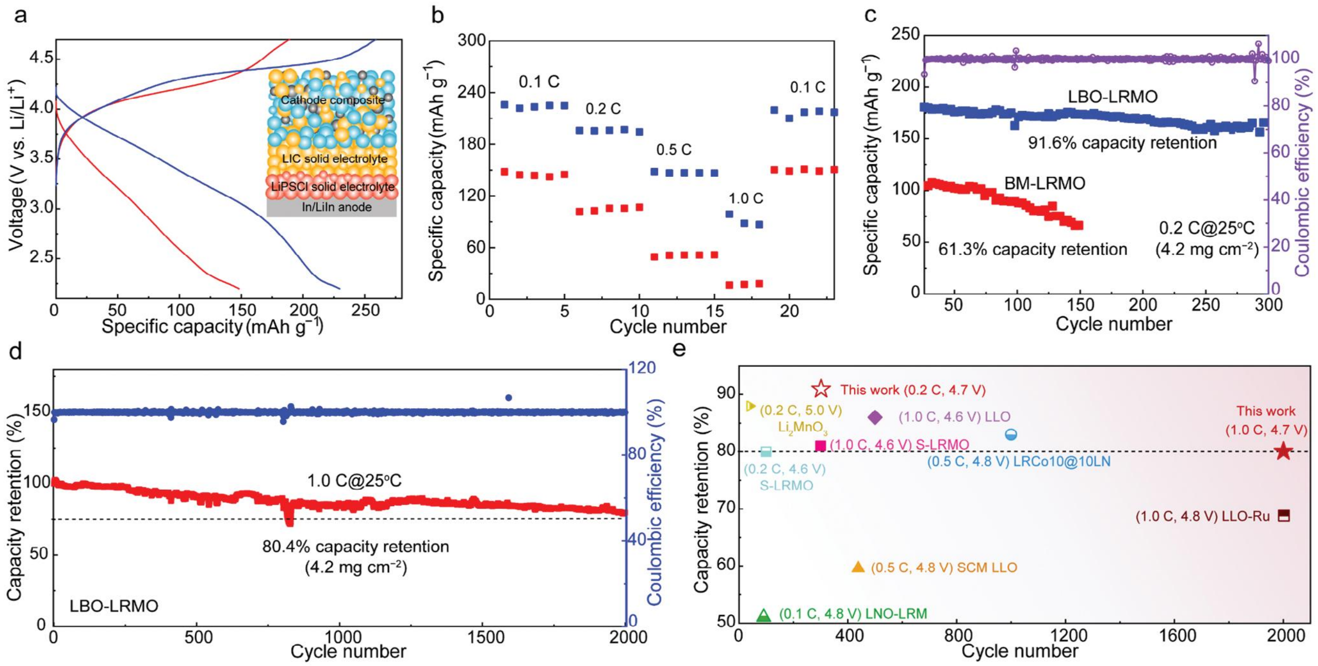

Figure 4. The electrochemical performance. a) The initial galvanostatic charge/ discharge voltage curves of BM-LRMO and LBO-LRMO ASSBs. b) The rate capability at various current densities. c) The cycling performance comparison of BM-LRMO and LBO-LRMO ASSBs at 0.2 C at 25 °C. d) The long-term cycling of LBO-LRMO ASSB at the current density of 1.0 C. e) Comparison of the cycling performance between previously reported LRMO ASSBs and the current study.[7,8,15,16,39,40]

spatial distribution of BO^- and MnO^- species within the LBO-LRMO matrix. The depth profiles shown in Figure S11d (Supporting Information) demonstrate a regular distribution of BO^- and MnO^- fragments, extending to depths of ≈500 nm, thus confirming the uniformity of B^{3+} throughout the material. All the above characterizations confirm the successful construction of the strong B–O bonds and high-efficiency ion pathways of amorphous LBO in cathodes.

In addition, in situ XRD measurements were conducted to monitor the real-time evolution of the LBO-LRMO crystal structure. The overall XRD patterns for the LBO-LRMO are shown in Figure S12a,b (Supporting Information). The key diffraction peaks, indexed as (003) and (101) are highlighted, as depicted in Figure S12c,d (Supporting Information). The peak corresponding interlayered spacing of (003) planes of polycrystalline LRMO shifts 0.21. This is much higher than the LBO-LRMO and previously reported value for the LRMO cathodes.[38] Moreover, the (101) peak for polycrystalline LRMO has undergone a significant shift toward higher degrees (0.30°), while there is only an extremely negligible deviation in the (101) peak of LBO-LRMO (0.13°) during the charge process, demonstrating the suppressed lattice variations of LBO-LRMO materials.[20]

2.3. Electrochemical Performance of LBO-LRMO Cathodes in ASSBs

The BM-LRMO and LBO-LRMO cathode composites were prepared by blending the cathode materials with commercial Li_3InCl_6 SEs and carbon nanotubes. The ASSBs were assembled by using PEEK cylinder solid cells, each containing a cathode composite, a combination of Li_3InCl_6 (LIC) and Li_6PS_5Cl (LPSC) SEs, and a Li-In anode. The ionic conductivity of both LIC and LPSC is 1.02 and 3.17 mS cm^{-1}, respectively (Figure S13, Supporting Information). Amorphous LBO contributes to the improved ionic conductivity of LBO-LRMO ($\approx 5.15 \times 10^{-7}$ mS cm^{-1}) compared to BM-LRMO ($\approx 7.65 \times 10^{-8}$ mS cm^{-1}) (Figure S14a,b, Supporting Information). Compared with the BM-LRMO ASSBs, the initial discharge capacity and Coulombic efficiency of LBO-LRMO are significantly improved after the synchronous gradient B doping and the integration of amorphous LBO. **Figure 4a** illustrates the initial charge/discharge voltage profile of BM-LRMO and LBO-LRMO-based ASSBs operating at a 0.1 C rate and a temperature of 25 ± 2 °C. The BM-LRMO-based ASSBs display a shortened charging plateau for anionic redox reactions, indicating sluggish Li-ion transport and suppressed anionic redox reactions in the Li_2MnO_3 phase during the first charge. This behavior is attributed to the high impedance at the Li_2MnO_3/LIC interface.[12] In contrast, the LBO-LRMO cathode exhibits a notably increased charging plateau for anionic redox reactions, suggesting significantly accelerated anionic redox kinetics after introducing the amorphous LBO networks. In addition, the initial Coulombic efficiency (ICE) for LBO-LRMO reaches 90%, substantially higher than that of the BM-LRMO electrode (78%), indicating B doping can effectively stabilize the oxygen configuration and improve the anionic redox reversibility. The rate capabilities for both BM-LRMO and LBO-LRMO are exhibited in Figure 4b. The LBO-LRMO-based ASSBs delivers a high initial discharge capacity of 231 mAh g^{-1} at the current

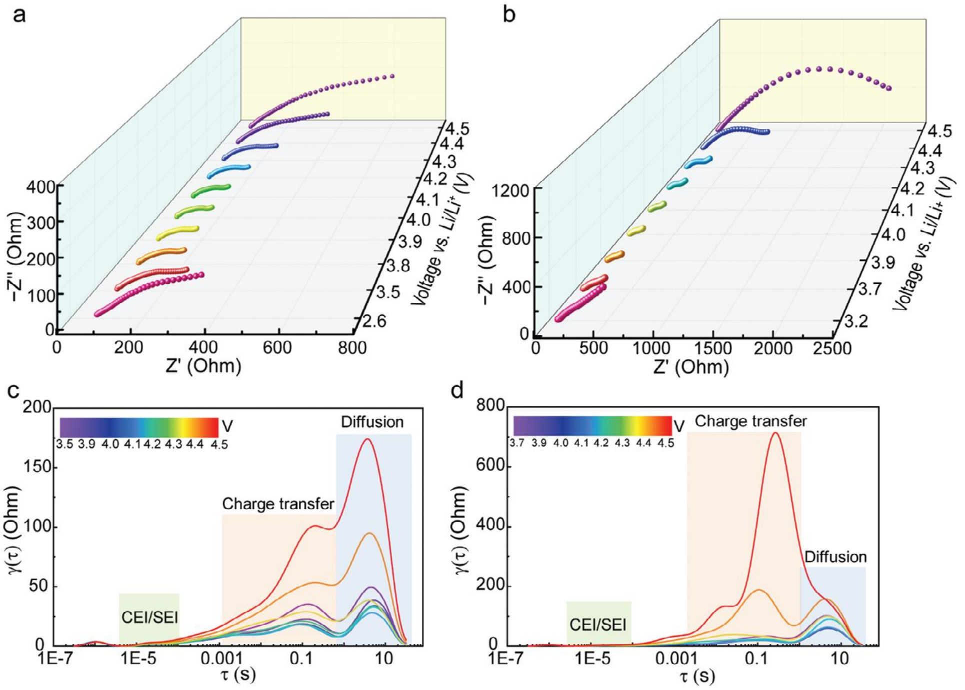

Figure 5. The interfacial kinetics analysis. a,b) The interfacial impedance change during the intial charge of the LBO-LRMO and BM-LRMO ASSBs between 2.2 and 4.7 V versus Li/Li$^+$. c,d) DRT profile transformation from GEIS of LBO-LRMO and BM-LRMO ASSBs, respectively.

density of 0.1C, whereas BM-LRMO-based ASSBs shows a much lower capacity (148 mAh g^{-1}). As the current density increases to 1.0 C, the LBO-LRMO still maintains a much higher specific capacity of 99 mAh g^{-1} (≈43% capacity retention) than that of BM-LRMO (19 mAh g^{-1} at 1.0 C, ≈13% capacity retention). The enhanced rate capability of LBO-LRMO can be attributed to the formation of the densely intertwined LRMO|LBO interfaces, where the amorphous LBO serves as the bridge to accelerate the Li-ion transport across the interior phase and LRMO|SEs interfaces.

The cycling performance of BM-LRMO and LBO-LRMO cathodes is depicted in Figure 4c. The LBO-LRMO ASSB demonstrates excellent stability, with only minor capacity decay, retaining 91.6% capacity over 300 cycles at 0.2 C. In contrast, the BM-LRMO ASSB experiences rapid capacity fade, with ≈80% capacity retention over 109 cycles, which is due to severe oxygen loss and interfacial degradation between the LBO-LRMO and SE. Impressively, when subjected to prolonged cycling at 1.0 C (Figure 4d), the LBO-LRMO ASSB maintains 80.4% capacity after 2000 cycles. This performance substantially exceeds that of previously reported LRMO-based ASSBs (Table S3, Supporting Information), including Li- and Mn-rich cathodes,[15,39,40] Li_3PO_4-coated LRMO,[16] the sulfidation of Ruthenium-doped LRMO,[7] and sulfite-modified LRMO.[8] Additionally, voltage decay, a critical issue that limits the industrial application of LRMO cathodes, is significantly suppressed in ASSBs utilizing the LBO-LRMO cathode composites. As shown in Figure S15 (Supporting Information), the voltage decay rate is ≈0.22 mV/cycle, which is better than that of reported Li-rich cathode materials,[38,41–43] indicating the stabilized oxygen configuration in LBO-LRMO.

2.4. Improved Anionic Redox Kinetics and Reversibility

Assessing interfacial kinetics and stability is crucial for understanding the behavior of anionic redox in ASSBs. Interfacial kinetics can be evaluated by the electrochemical impedance spectroscopy (EIS) measurements in combination with distribution of relaxation time (DRT) analysis. The EIS analysis was conducted over a frequency range from 0.01 Hz to 1.00 MHz, utilizing a 5 mV amplitude on a Solartron EnergyLab XM workstation. **Figure** 5a,b illustrates the impedance progression of the LBO-LRMO and BM-LRMO ASSBs at various cutoff voltages. It has been reported that compared to the charge-transfer resistance (R_{ct}) through anode/SSE ($R_{anode|SE}$), the cathode|SE interfacial resistance ($R_{cathode|SE}$) dominates the whole resistance evolution.[8] Consequently, the significant increase in the charge transfer resistance observed as the voltage increases from the open-circuit voltage (OCV) to 4.7 V versus Li/Li$^+$ is primarily attributed to the working cathode|SE interfaces. Notably, such a significant increase of R_{ct}, predominantly occurring above 4.3 V, is associated with the anionic redox process,[44] indicating the sluggish Li-ion transport kinetics between the Li_2MnO_3 and SEs within BM-LRMO ASSBs. In stark contrast, the LBO-LRMO ASSB, as shown in Figure 5b, displays a considerably smaller variation in R_{ct}, even above 4.3 V. This implies the significantly reduced impedance between the Li_2MnO_3 and SEs, and improved anionic redox kinetics within LBO-LRMO ASSBs.

In addition, DRT technology is also used to decouple the resistance evolution in cathode composites during the charge/discharge process. The relaxation time τ in the DRT profiles represents the specific electrochemical process. According to the different relaxation times of each electrochemical process,

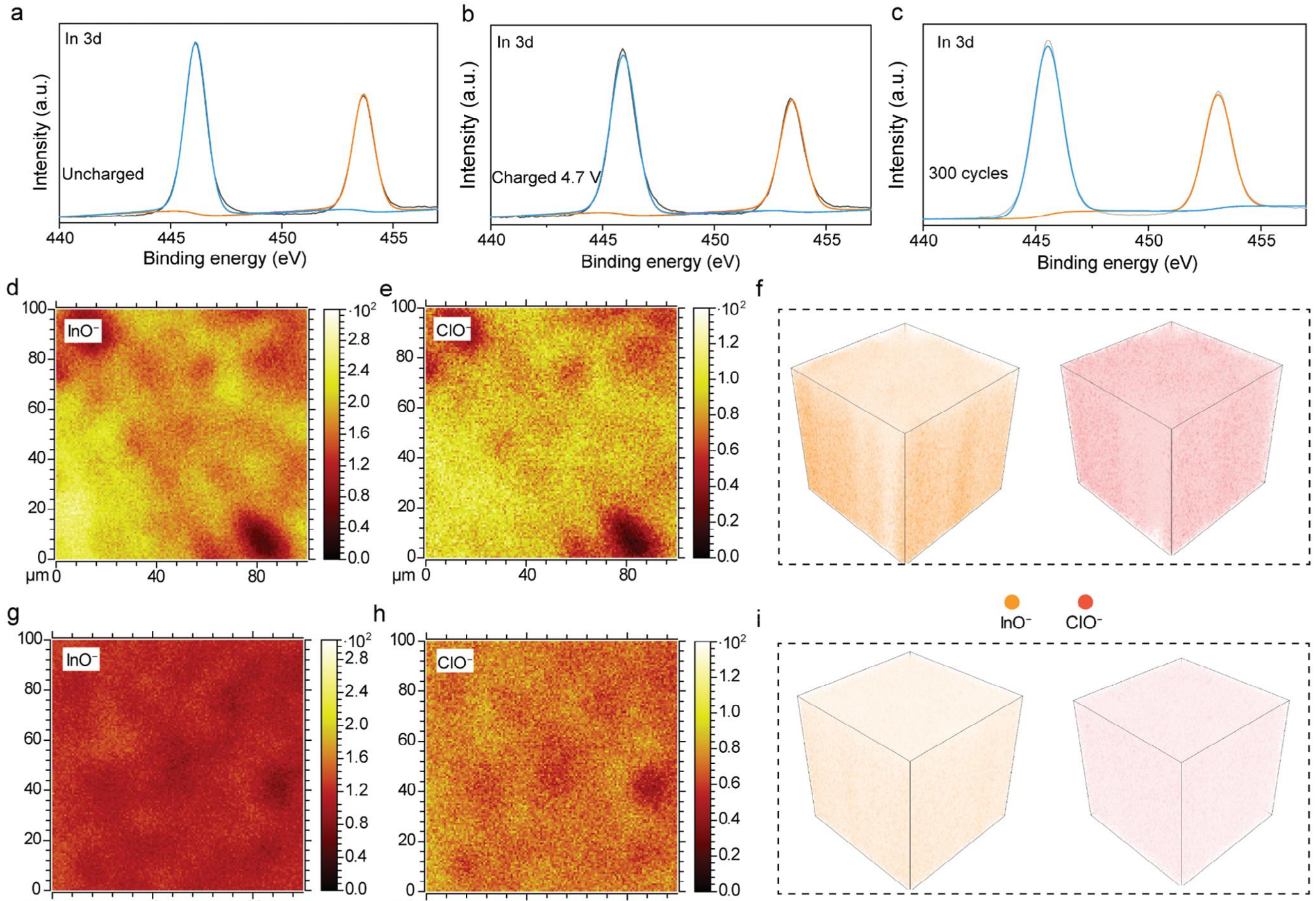

Figure 6. The interfacial chemical evolution analysis. a,b) In 3d XPS spectra for the LBO-LRMO collected at uncharged and charged (4.7 V vs Li/Li$^+$). c) In 3d XPS spectra for the LBO-LRMO collected after 300 cycles. d,e) Time-of-flight secondary ion mass spectrometry (TOF-SIMS) images of ClO$^-$ and InO$^-$ species in cycled BM-LRMO cathode composites (300th cycles). The color bar exhibits the intensity of the ion fragment signals. f) TOF-SIMS 3D images of the InO$^-$ and ClO$^-$ species in cycled BM-LRMO. g,h) TOF-SIMS images of ClO$^-$ and InO$^-$ species in cycled LBO-LRMO cathode composites (300th cycles). i) TOF-SIMS 3D images of the InO$^-$ and ClO$^-$ species in cycled LBO-LRMO cathode composites.

three main regions can be distinguished in DRT plots, including CEI/SEI, charge transfer, and diffusion (Figure 5c,d).[45,46] It is apparent that the R$_{ct}$ increases sharply at the BM-LMRO|SE interface (Figure 5d) over 4.3 V, especially for the τ at ≈10^{-1} s, which represents the response of the Li$_2$MnO$_3$|SE interface. Such high interfacial impedance over 4.3 V severely hinders the anionic redox process consistent with the charge/discharge results. In contrast, the LBO-LMRO|SE interface maintains a low resistance value (R$_{ct}$, τ from 10^{-3}–1 s) even at the high voltage of 4.7 V, indicating the fast Li-ion transport kinetics after introducing B–O bonds and ionic networks in LRMO cathodes.[8,46] During the discharging process (Figure S16, Supporting Information), the interface in BM-LRMO cathode composites still maintains relatively higher resistance than that in LBO-LRMO cathode composites, further verifying the significant influence of the nanoscale LBO composites on the interfacial kinetics and stability. To further quantify the chemical diffusion coefficient of lithium (D_{Li+}) of the electrode, GITTs were employed in both BM-LRMO and LBO-LRMO electrodes during the charging process. As shown in Figure S17 (Supporting Information), the D_{Li+} values for LBO-LRMO and BM-LRMO are comparable below 4.3 V, ranging from 10^{-9} to 10^{-11} cm^2 s^{-1}. However, once the voltage exceeds 4.3 V, the D_{Li+} for LBO-LRMO (ranging from 10^{-10} to 10^{-12} cm^2 s^{-1}) is one to two orders of magnitude higher than that of BM-LRMO (ranging from10^{-11} to 10^{-14} cm^2 s^{-1}).

In order to demonstrate the interfacial compatibility between the cathode and SE, ex situ XPS was carried out to monitor the interfacial chemical evolution. **Figure 6a–c** displays the XPS spectra of In 3d for the cycled LBO-LRMO composite cathode at different states. When the LBO-LRMO composite cathode is charged to 4.7 V (Figure 6a,b), no new peak indicative of indium-based oxides is observed.[47] Even after 300 cycles, the O-involving degradation of LIC is not aggravated (Figure 6c), demonstrating the outstanding reversibility of anionic redox reactions after the B—O bond introduction.[48] In addition to the XPS analyses, TOF-SIMS measurements are performed to obtain further information on the anionic redox reversibility. The cycled BM-LRMO composite cathode was compared to the LBO-LRMO composite cathode (Figure S18, Supporting Information), both of which were prepared in the same way after 300 cycles. The color bar exhibits the intensity of the ion fragment signals.[49,50] The high signals of InO$^-$ and ClO$^-$ fragments are evidence of the interfacial

O-involving degradation, which derives from the anionic redox irreversibility of LRMO and the subsequently caused oxidation of halide SEs. As shown in Figure 6d,e, the InO^- and ClO^- fragments collected from cycled BM-LRMO composite cathode display strong intensity, revealing the continuously growing degradation layers during the cycling. 3D reconstructions (Figure 6f; Figure S19, Supporting Information) further confirm the generation of abundant InO^- and ClO^-, which are uniformly distributed throughout the cycled BM-LRMO cathode composites. In sharp contrast, the LBO-LRMO cathodes with highly reversible anionic reactions exhibit slightly increased signal intensities of InO^- and ClO^- fragments even after 300 cycles (Figure 6g,h), demonstrating the highly stable oxygen configuration after introducing B–O bonds. 3D reconstructions (Figure 6i; Figure S20, Supporting Information) also confirm the homogeneous doping of B^{3+} in the bulk and the low-intensity InO^- and ClO^- fragments in the cycled LBO-LRMO cathode composites.

The morphological evolution of the BM-LRMO and LBO-LRMO composite interfaces after 300 cycles was examined by SEM and corresponding EDS (Figures S21 and S22, Supporting Information). Figure S21 (Supporting Information) reveals that cathode materials are surrounded by a matrix consisting of LIC and carbon nanotubes in cycled BM-LRMO and LBO-LRMO cathode composites. Cracking is observed in the cycled BM-LRMO cathode composite, whereas no significant cracks are formed in the LBO-LRMO cathode composite after 300 cycles. This improvement is attributed to the reduced lattice deformation and the stabilizing effect of the well-connected soft LBO networks. As shown in the cross-section SEM image of the ASSBs (Figure S22, Supporting Information), owing to the LIC SE affords close contact with the cycled LBO-LRMO electrode, guaranteeing efficient charge transfer at the interface with low interfacial impedance.

3. Conclusion

The anionic redox activity and reversibility of LBO-LRMO in ASSBs were significantly enhanced through the one-step integration of 3D Li-ion networks and B-doping within the LRMO cathode materials. Theoretical calculations, coupled with multiscale in situ and ex situ experimental characterizations, have elucidated a marked improvement in anionic redox reactions. This enhancement is attributed to two synergistic factors: 1) the incorporation of heterogenous B^{3+} cations into LRMO effectively reduces the bond length of TM–O covalence and therefore suppresses lattice oxygen escape; 2) the embedded 3D LBO ionic networks in LRMO serve as a bridge to accelerate the Li-ion transport between the Li_2MnO_3 phase and SE interface, therefore stimulating the anionic redox reactions. Consequently, the as-prepared LBO-LRMO cathode retains 80.4% of its initial discharge capacity after 2000 cycles at a current density of 1.0 C, outperforming previously reported LRMO-based ASSBs. Our discovery presents an effective strategy for the rational design of cathodes that promote high-efficiency cationic and anionic redox reactions, leading to ASSBs with superior cycle life and energy density.

4. Experimental Section

Materials Synthesis: *Synthesis of BM-LRMO and LBO-LRMO Materials*: Pristine LRMO was fabricated by coprecipitation as reported previously.[51] The pristine LRMO were added into a zirconia pot with a powder–to–ball mass ratio of 1:20. The milling process was carried out in a planetary apparatus (MITR, QM–QX–0.4 L) at 500 rpm for 60 h in Ar atmosphere to achieve BM-LRMO. Furthermore, 20% LBO were mixed with 80% pristine LRMO by the high-energy mechanical milling. The as-obtained sample was further annealed at 400 °C for 4 h to prepare LBO-LRMO cathodes.[31]

Material Characterization: Scanning electron microscopy (SEM) with a JSM 7401F was utilized to examine the morphology and cross-sections of the materials. The structure of the cathode materials was determined using X-ray diffraction (XRD) on a Bruker D8 diffractometer, with subsequent Rietveld refinement performed using GSAS II software. Surface and interface chemistry were analyzed by X-ray photoelectron spectroscopy (XPS) with an Al K_α source on a Kratos Analytical Axis Supra+ and time-of-flight secondary ion mass spectrometry (TOF-SIMS) on an ION-TOF GmbH 5–100, respectively. The atomic structure characterization was conducted using aberration-corrected scanning transmission electron microscopy on a FEI Titan Cubed Themis G2 300 operated at 300 kV.

Electrochemical Measurements: Both LIC Sand LPSC SEs were provided by Nanjing Suzhan Intelligent Technology Co., Ltd. The solid battery molds were purchased from Nanjing Jincaixin Technology Co., Ltd. The ASSBs employing the BM-LRMO and LBO-LRMO in combination with the LIC SE and the In/InLi anode were assembled in the glovebox. The mass loading of the active materials is 4.2 mg cm^{-2}. The LPSC with high stability with the anode was added between the anode and LIC to inhibit the side reactions. First, 40 mg LPSC was added into the solid battery molds and pressed at 360 MPa for 2 min. Then 40 mg of LIC was pressed on the LPSC thin film with the same condition. The cathode composite was prepared by blending cathodes with carbon nanotubes and LIC SEs with a weight ratio of 60:5:40 and was pressed at 360 MPa for 3 min. Following, an In foil (0.10 mm thickness, 10 mm diameter) was pressed on the other side and then a thin Li foil (0.03 mm thickness, 10 mm diameter) was pressed on the In foil. Finally, this ASSB cell was fixed into a stainless-steel plate casing with a stack pressure of 20 MPa.

The Galvanostatic charge/discharge of the ASSB was operated ranging from 2.2 to 4.7 V versus Li/Li^+ at different rates using Land battery test system (Wuhan Land Electronic Co. Ltd., China). The Solartron Energy Lab XM is used to collect the in situ EIS spectra. The frequency ranges from 1 MHz to 0.01 Hz and the amplitude is 10 mV. The repetitive GEIS measurements are conducted during the charging and discharging process after an equal interval time of 0.5 h. In addition, the DRT analyses are transited by the MATLAB GUI toolbox that was developed by Ciucci's research team.[52] The chemical diffusion is characterized by the GITT, in which the relaxations in cathode materials originate from the Li^+ diffusion. The diffusion coefficient is calculated by the following Equations (1) and (2)

$$D_{GITT} = \frac{4}{\pi\tau}\left(\frac{n_m V_m}{S}\right)^2\left(\frac{\Delta E_s}{\Delta E_t}\right)^2 \tag{1}$$

$$\tau \ll \frac{L^2}{D_{GITT}} \tag{2}$$

where τ represents relaxation time, n_m is the mole value, V_m represents the mole volume, S represents the contact area of cathode/SE, ΔEs represents the voltage response under the pulse current, and ΔEt is the voltage change through the galvanostatic discharge.

Density Functional Theory Calculation: Density functional theory (DFT) calculations were performed to reveal the stabilization mechanism of layered Li_2MnO_3 induced by the pinning effect using the Vienna ab initio Simulation Package (VASP). The projector-augmented wave (PAW) method was used to describe the ion-electron interactions. Perdew–Burke–Ernzerhof (PBE) version of generalized gradient approximation (GGA) was adopted for the exchange-correlation energy. A kinetic energy cutoff of 520 eV was used for the plane wave expansion of the valence electron wave functions. A dense Γ-centered Monkhorst-Pack k-point mesh with a sampling density of 0.04 $Å^{-1}$, 10^{-6} eV/cell in total energy, and

10^{-2} eV Å^{-1} in force was adopted for the convergence criterion during structural optimization. Because of the layered structure, van der Waals (vdW) density functional of optB86b-vdW functional was performed during structural optimization. Considering the strong electron correction effect in transition-metal oxides, electronic structure calculations were performed by a GGA plus Hubbard U (GGA + U). A U value of 4.5 eV was set for the d electrons in Mn atoms. A Li_2MnO_3(010) surface model was constructed based on the experimental XRD data. A vacuum layer of 15 Å was set to avoid the artificial interlayer interaction due to the periodic boundary condition.

Supporting Information

Supporting Information is available from the Wiley Online Library or from the author.

Acknowledgements

This work was supported by the National Key Research and Development Program (2021YFB2500300), the Beijing Municipal Natural Science Foundation (Z200011 and L233004), the National Natural Science Foundation of China (22209092, 22393900, 22393904, 22108151, 22308190, 22209094, 52394170, 22393903, and T2322015), the Natural Science Foundation of Jiangsu Province (SBK2024022826), the China Postdoctoral Science Foundation (2023M731864, 2023M731920, 2023M741922, and 2022TQ0165), Tsinghua University Initiative Scientific Research Program, and the "Shuimu Tsinghua Scholar Program of Tsinghua University".

Conflict of Interest

The authors declare no conflict of interest.

Data Availability Statement

The data that support the findings of this study are available from the corresponding author upon reasonable request.

Keywords

3D LBO ionic networks, all-solid-state batteries, anionic redox reactions, lithium-rich manganese-based oxides, long-term cycling stability

Received: September 19, 2024
Revised: December 12, 2024

---

[1] J. Janek, W. G. Zeier, *Nat. Energy* **2023**, *8*, 230.
[2] Y. Su, X. Rong, H. Li, X. Huang, L. Chen, B. Liu, Y. S. Hu, *Adv. Mater.* **2023**, *35*, 2209402.
[3] L. Ye, Y. Lu, Y. Wang, J. Li, X. Li, *Nat. Mater.* **2024**, *23*, 244.
[4] S. Kalnaus, N. J. Dudney, A. S. Westover, E. Herbert, S. Hackney, *Science* **2023**, *381*, eabg5998.
[5] J.-J. Marie, R. A. House, G. J. Rees, A. W. Robertson, M. Jenkins, J. Chen, S. Agrestini, M. Garcia-Fernandez, K.-J. Zhou, P. G. Bruce, *Nat. Mater.* **2024**, *23*, 818.
[6] W. J. Kong, C. Z. Zhao, S. Sun, L. Shen, X. Y. Huang, P. Xu, Y. Lu, W. Z. Huang, J. Q. Huang, Q. Zhang, *Adv. Mater.* **2024**, *36*, 2310738.
[7] Y. Wang, D. Wu, P. Chen, P. Lu, X. Wang, L. Chen, H. Li, F. Wu, *Adv. Funct. Mater.* **2024**, *34*, 2309822.
[8] S. Sun, C.-Z. Zhao, H. Yuan, Z.-H. Fu, X. Chen, Y. Lu, Y.-F. Li, J.-K. Hu, J. Dong, J.-Q. Huang, *Sci. Adv.* **2022**, *8*, eadd5189.
[9] I. Konuma, D. Goonetilleke, N. Sharma, T. Miyuki, S. Hiroi, K. Ohara, Y. Yamakawa, Y. Morino, H. B. Rajendra, T. Ishigaki, *Nat. Mater.* **2023**, *22*, 225.
[10] A. M. Pillai, P. S. Salini, G. R. Krishnan, A. Chithra, B. John, S. Pillai, S. SarojiniAmma, M. T. Devassy, *J. Alloys Compd.* **2024**, *976*, 173064.
[11] N. Hu, Y. H. Zhang, Y. Yang, H. Wu, Y. Liu, C. Hao, Y. Zheng, D. Sun, W. Li, J. Li, *Adv. Energy Mater.* **2024**, *14*, 2303797.
[12] B. Liu, N. Hu, C. Li, J. Ma, J. Zhang, Y. Yang, D. Sun, B. Yin, G. Cui, *Angew. Chem., Int. Ed.* **2022**, *134*, e202209626.
[13] J. Zhao, Y. Su, J. Dong, X. Wang, Y. Lu, N. Li, Q. Huang, J. Hao, Y. Wu, B. Zhang, *J. Energy Chem.* **2024**, *98*, 274.
[14] K. Kawai, X.-M. Shi, N. Takenaka, J. Jang, B. M. de Boisse, A. Tsuchimoto, D. Asakura, J. Kikkawa, M. Nakayama, M. Okubo, *Energy Environ. Sci.* **2022**, *15*, 2591.
[15] K. Hikima, K. Shimizu, H. Kiuchi, Y. Hinuma, K. Suzuki, M. Hirayama, E. Matsubara, R. Kanno, *J. Am. Chem. Soc.* **2021**, *144*, 236.
[16] R. Yu, C. Wang, H. Duan, M. Jiang, A. Zhang, A. Fraser, J. Zuo, Y. Wu, Y. Sun, Y. Zhao, *Adv. Mater.* **2023**, *35*, 2207234.
[17] D. Luo, H. Zhu, Y. Xia, Z. Yin, Y. Qin, T. Li, Q. Zhang, L. Gu, Y. Peng, J. Zhang, *Nat. Energy* **2023**, *8*, 1078.
[18] X. Xu, S. Chu, S. Xu, S. Guo, H. Zhou, *Energy Environ. Sci.* **2024**, *17*, 3052.
[19] Y. Fang, Y. Su, J. Dong, J. Zhao, H. Wang, Y. Lu, B. Zhang, H. Yan, F. Wu, L. Chen, *J. Energy Chem.* **2024**, *92*, 250.
[20] Y. Yang, C. Gao, T. Luo, J. Song, T. Yang, H. Wang, K. Zhang, Y. Zuo, W. Xiao, Z. Jiang, *Adv. Mater.* **2023**, *35*, 2307138.
[21] J. Yang, P. Li, F. Zhong, X. Feng, W. Chen, X. Ai, H. Yang, D. Xia, Y. Cao, *Adv. Energy Mater.* **2020**, *10*, 1904264.
[22] S. Liu, Z. Liu, X. Shen, W. Li, Y. Gao, M. N. Banis, M. Li, K. Chen, L. Zhu, R. Yu, *Adv. Energy Mater.* **2018**, *8*, 1802105.
[23] T. Wu, X. Liu, X. Zhang, Y. Lu, B. Wang, Q. Deng, Y. Yang, E. Wang, Z. Lyu, Y. Li, *Adv. Mater.* **2021**, *33*, 2001358.
[24] K. McColl, S. W. Coles, P. Zarabadi-Poor, B. J. Morgan, M. S. Islam, *Nat. Mater.* **2024**, *23*,826.
[25] X. Han, R. Wu, G. Gao, J. Li, M. Fan, S. Wang, Y. Liu, S. Li, L. Lin, Y. Zhang, *ACS Energy Lett.* **2024**, *9*, 3219.
[26] Y. Liu, H. Zhu, H. Zhu, Y. Ren, Y. Zhu, Y. Huang, L. Dai, S. Dou, J. Xu, C. J. Sun, *Adv. Energy Mater.* **2021**, *11*, 2003479.
[27] M. Akhilash, P. Salini, B. John, S. Sujatha, T. Mercy, *Chem. Rec.* **2023**, *23*, e202300132.
[28] Y.-J. Guo, P.-F. Wang, Y.-B. Niu, X.-D. Zhang, Q. Li, X. Yu, M. Fan, W.-P. Chen, Y. Yu, X. Liu, *Nat. Commun.* **2021**, *12*, 5267.
[29] J. Chen, H. Chen, Y. Mei, J. Gao, A. Dai, Y. Tian, W. Deng, G. Zou, H. Hou, C. E. Banks, *Energy Storage Mater.* **2022**, *52*, 736.
[30] B. Li, H. Yan, J. Ma, P. Yu, D. Xia, W. Huang, W. Chu, Z. Wu, *Adv. Funct. Mater.* **2014**, *24*, 5112.
[31] S. Takei, A. Itoh, Y. Kobayashi, K. Kamata, S. Yasui, *J. Appl. Phys.* **2023**, *62*, SM1025.
[32] D. Button, L. Mason, H. Tuller, D. Uhlmann, *Solid State Ion* **1983**, *9*, 585.
[33] D. Wohlmuth, V. Epp, B. Stanje, A. M. Welsch, H. Behrens, M. Wilkening, *J. Am. Ceram. Soc.* **2016**, *99*, 1687.
[34] Z. Dai, H. Zhao, W. Chen, Q. Zhang, X. Song, G. He, Y. Zhao, X. Lu, Y. Bai, *Adv. Funct. Mater.* **2022**, *32*, 2206428.
[35] T. Liu, J. Liu, L. Li, L. Yu, J. Diao, T. Zhou, S. Li, A. Dai, W. Zhao, S. Xu, *Nature* **2022**, *606*, 305.
[36] J.-H. Jeong, D.-w. Jung, E. W. Shin, E.-S. Oh, *J. Alloys Compd.* **2014**, *604*, 226.
[37] N. Feng, Q. Wang, A. Zheng, Z. Zhang, J. Fan, S.-B. Liu, J.-P. Amoureux, F. Deng, *J. Am. Chem. Soc.* **2013**, *135*, 1607.
[38] Y. H. Zhang, D. Zhang, L. R. Wu, J. Ma, Q. Yi, Z. Wang, X. Wang, Z. Wu, C. Zhang, N. Hu, *Adv. Energy Mater.* **2022**, *12*, 2202341.

[39] W. Du, Q. Shao, Y. Wei, C. Yan, P. Gao, Y. Lin, Y. Jiang, Y. Liu, X. Yu, M. Gao, *ACS Energy Lett.* **2022**, *7*, 3006.

[40] C. Zhang, Z. Lu, M. Song, Y. Zhang, C. Jing, L. Chen, X. Ji, W. Wei, *Adv. Energy Mater.* **2023**, *13*, 2203870.

[41] J. Zhang, Q. Zhang, D. Wong, N. Zhang, G. Ren, L. Gu, C. Schulz, L. He, Y. Yu, X. Liu, *Nat. Commun.* **2021**, *12*, 3071.

[42] Z. Zhu, D. Yu, Y. Yang, C. Su, Y. Huang, Y. Dong, I. Waluyo, B. Wang, A. Hunt, X. Yao, *Nat. Energy* **2019**, *4*, 1049.

[43] D. Eum, B. Kim, S. J. Kim, H. Park, J. Wu, S.-P. Cho, G. Yoon, M. H. Lee, S.-K. Jung, W. Yang, *Nat. Mater.* **2020**, *19*, 419.

[44] X. Wang, Q. Zhang, C. Zhao, H. Li, B. Zhang, G. Zeng, Y. Tang, Z. Huang, I. Hwang, H. Zhang, *Nat. Energy* **2024**, *9*, 184.

[45] Y. Lu, C.-Z. Zhao, J.-Q. Huang, Q. Zhang, *Joule* **2022**, *6*, 1172.

[46] Y. Lu, C.-Z. Zhao, J.-K. Hu, S. Sun, H. Yuan, Z.-H. Fu, X. Chen, J.-Q. Huang, M. Ouyang, Q. Zhang, *Sci. Adv.* **2022**, *8*, eadd0510.

[47] C. Wang, J. Liang, M. Jiang, X. Li, S. Mukherjee, K. Adair, M. Zheng, Y. Zhao, F. Zhao, S. Zhang, *Nano Energy* **2020**, *76*, 105015.

[48] A. Zhang, J. Wang, R. Yu, H. Zhuo, C. Wang, Z. Ren, J. Wang, *ACS Appl. Mater. Interfaces* **2023**, *15*, 8190.

[49] F. Walther, R. Koerver, T. Fuchs, S. Ohno, J. Sann, M. Rohnke, W. G. Zeier, J. R. Janek, *Chem.Mater* **2019**, *31*, 3745.

[50] L. Shen, J. L. Li, W. J. Kong, C. X. Bi, P. Xu, X. Y. Huang, W. Z. Huang, F. Fu, Y. C. Le, C. Z. Zhao, *Adv. Funct. Mater.* **2024**, 2408571.

[51] S. Hu, Y. Li, Y. Chen, J. Peng, T. Zhou, W. K. Pang, C. Didier, V. K. Peterson, H. Wang, Q. Li, *Adv. Energy Mater.* **2019**, *9*, 1901795.

[52] T. H. Wan, M. Saccoccio, C. Chen, F. Ciucci, *Electrochim. Acta* **2015**, *184*, 483.